Acta Cryst. (1996). A**52**, 302–311

Bragg-Case X-ray Interference in Multilayered Structures. Comparison Between Kinematical Approximation and Dynamical Treatment

A. PARISINI,* S. MILITA AND M. SERVIDORI

CNR–Istituto LAMEL, Via Gobetti 101, I–40129 Bologna, Italy. E-mail: parisini@area.bo.cnr.it

(Received 8 September 1995; accepted 16 November 1995)

Abstract

A kinematical model is proposed to describe X-ray interference phenomena in the symmetric Bragg case from multilamina structures. The formalism is able to represent any desired sequence of crystalline and non-diffracting layers and hence can be used for a variety of experimental situations from heterostructures to implanted single crystals with embedded amorphous layers. Owing to the relevant thicknesses involved in the implant, the analysis of the interference effects by this model is not restricted to the case of very thin embedded layers commonly encountered in heterostructure-based optoelectronic devices. The model is hence of more general validity. Comparison with rocking curves obtained by dynamical treatment of experimental data, relative to silicon implanted in such conditions as to produce buried amorphous layers, shows that all the interference features are well reproduced by the model.

1. Introduction

Bragg-case X-ray interference phenomena accompanying diffraction from multilayered heterostructures are receiving particular attention owing to the interest of these materials in electronic and optoelectronic device manufacturing. The relevance of these studies resides in the determination of lattice strain, mismatch, composition, degree of relaxation and thickness of the layers with high accuracy. Among the various layer structures producing such interference effects, quantum wells, lasers and high-electron-mobility transistors were investigated in the recent past (see *e.g.* Tapfer & Ploog, 1989; Wie, Chen, Kim, Liu, Choi & Hwang, 1989; Holloway, 1990; Tanner, 1993), mainly to correlate the modulations in X-ray diffraction curves to the structural properties of the constituent layers, also as thin as one monolayer. However, other sandwich structures, obtained for instance by ion implantation, are relevant from the technological point of view and deserve the same degree of attention. In the last few years, silicon-on-insulator (SOI) structures have been fabricated by separation by implanted oxygen (SIMOX) and suitable high-temperature thermal cycles (Jaussaud, Stoemenos, Margail, Papon & Bruel, 1991; Margail, Lamure & Papon, 1992; Nikulin, Snigirev, Starkov, Hemment & Vyatkin, 1992). These structures include buried amorphous silicon oxide layers and then produce well defined interference effects when rocked around their Bragg peak, provided that the crystal quality of the cladding layers is sufficiently perfect. Hence, the analysis of the interference patterns enables the assessment of layer perfection in SOI structures.

The difficulty in obtaining SOI structures of good lattice regularity by SIMOX made us limit our interest to the analysis of Bragg-case X-ray interference phenomena occurring between crystalline regions separated by non-diffracting (amorphous) material as produced in as-implanted silicon crystals. In this paper, a kinematical description is proposed for such an analysis. Owing to the relevant surface layer thicknesses involved in the implant, this description will necessarily be somewhat different from those reported by Holloway (1990) and Tapfer & Ploog (1989). In fact, in these papers, Bragg-case interference effects were studied from structures including such thin crystalline layers that diffraction from them could be neglected and some approximations in the kinematical treatment are allowed. However, in our case of thicker non-diffracting layers, certain approximations have to be removed. The formalism presented here will then be of more general validity. Calculations obtained by these kinematical expressions will be compared with experimental data for ion-implanted silicon resulting from analysis with a dynamical model.

2. Kinematical approximation

2.1. *Perfect crystal*

Resorting to the kinematical approximation, which enables an easy analytical description of the diffraction phenomenon, has already been used not only in the case of multilayered heterostructures (Tapfer & Ploog, 1989; Wie, 1989; Holloway, 1990; Wie & Kim, 1991) but also in diffused and ion-implanted crystals (Afanas'ev, Koval'chuk, Kovev & Kohn, 1977; Speriosu, 1981). The main interest in this description relies on the possibility of clarifying the relative importance of the different structural parameters responsible for the complicated interference pattern experimentally observed in multilayered materials. The use of this single-scattering approximation is allowed if the sample thickness is con-

siderably smaller than the X-ray extinction length. Only in this case are dynamical and kinematical calculations equivalent. In what follows, we will apply the kinematical approximation in the Bragg case to the analysis of double-crystal X-ray rocking curves (RCs) resulting from implanted samples containing an embedded amorphous layer. In this case, reflectivity modulations are expected as a result of the interference of the two crystalline regions separated by the non-diffracting layer. It is worth noting that this situation is very similar to that observed in the case of multilayered heterostructures, where the Bragg peak of a thin separating layer is far away from the ones of the interfering regions.

Our starting point is the optical approach to the kinematical theory (James, 1967). In this context, the reflectivity of a crystal slab consisting of p parallel planes with spacing d is obtained by considering the interference among p reflected waves whose amplitude q (complex for an absorbing crystal) is given by the Darwin amplitude scattered by each plane and with phase differences between waves scattered by two successive planes given by $\delta = (4\pi/\lambda)d\sin(\theta)$. For a σ-polarized incident wave and neglecting refraction, this reflectivity is given by

$$R(\theta) = |q|^2 \sin^2(p\delta/2)/\sin^2(\delta/2), \qquad (1)$$

where $q = -[\lambda d/(V\sin\theta)]Fr_e$, λ is the X-ray wavelength, V the unit-cell volume, θ the incidence angle, F the structure factor and r_e the classical electron radius. The right-hand side of (1) is essentially an interference function. This can be made even more evident with the following rearrangement of (1). Let us consider a perfect crystal with p parallel reflecting planes composed of two layers consisting of p_1 and p_2 planes, respectively, as schematically shown in Fig. 1(*a*). By inserting $p = p_1 + p_2$ in (1), after some handling we get

$$R(\theta) = R_1(\theta)+R_2(\theta)+2[R_1(\theta)R_2(\theta)]^{1/2}\cos[\alpha(\theta)], \qquad (2)$$

where

$$R_{1,2}(\theta) = |q|^2 \sin^2(p_{1,2}\delta/2)/\sin^2(\delta/2) \qquad (3)$$

and

$$\alpha(\theta) = (4\pi/\lambda)[(p_1 + p_2)d/2]\sin(\theta). \qquad (4)$$

Equation (2) has the form of a two-beam interference expression with intensity ratios R_1 and R_2 and phase difference α dependent on θ. The interference pattern will then consist of the fringes due to the terms of (3) and to cosinusoidal interference fringes modulated by the term $2[R_1(\theta)R_2(\theta)]^{1/2}$.

Therefore, in this framework, the crystal behaves just like an amplitude splitting interferometer and the interference pattern given by (1) or (2) can be thought of as due to two virtual coherent sources, S_1 and S_2, as shown in Fig. 1(*c*). In fact, with reference to this figure, the path difference between the normals to the wavefronts emitted by S_1 and S_2, neglecting beam deviations due to the different refractive indices in the crystal and in vacuum, is given by $\overline{S_2H} = 2\overline{A_1A_2}\sin(\theta)$, where $\overline{A_1A_2} = (p_1 + p_2)d/2$ corresponds to the distance between the mid-points, A_1 and A_2, of the two layers composing the crystal. This results in a phase difference $\alpha(\theta) = (2\pi/\lambda)\overline{S_2H}$, as given in (4).

The interest in this description is because it can be straightforwardly extended to the case of an embedded non-reflecting layer. In fact, let us take the two layers at a distance t apart, as shown in Fig. 1(*b*), and consider the optical analogue of the X-ray diffraction in Fig. 1(*d*). By comparing Figs. 1(*c*) and (*d*), it is seen that the only difference from the previous case is the value of the distance $\overline{A_1A_2}$, which is given here by $\overline{A_1A_2} = (p_1 + p_2)d/2 + t$. Therefore, the reflectivity will still be given by (2), where now $\alpha(\theta)$ will be given by the expression

$$\alpha(\theta) = (4\pi/\lambda)\overline{A_1A_2}\sin(\theta) = (4\pi/\lambda)[(p_1 + p_2)d/2 + t]\sin(\theta). \qquad (5)$$

This approach evidences the dependence of $\alpha(\theta)$ on the thickness t of the non-diffracting layer. This dependence can be described as follows. From (5), when the condition $(4\pi/\lambda)t\sin(\theta) = 2\pi n$ is satisfied for a given incidence angle, the reflectivity $R(\theta)$ at this angle will equal that in the absence of the non-diffracting layer, *i.e.* $R(\theta)$ will be the same as that resulting from (2) with $\alpha(\theta)$ given by (4). Thus, at a given incidence angle θ,

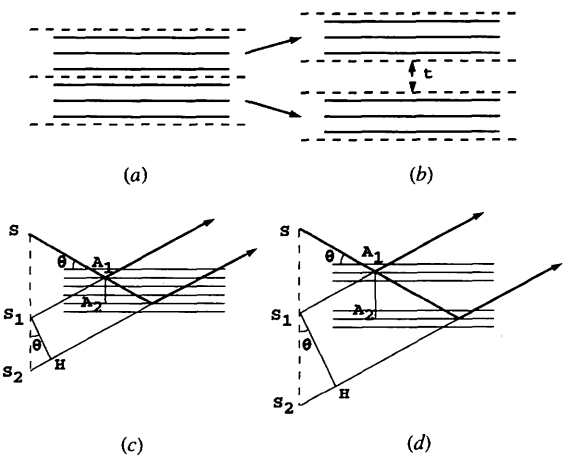

Fig. 1. Sketch of kinematical diffraction from a two-layer structure composed of $p_1 = p_2$ d-spaced lattice planes without (*a* and *c*) and with (*b* and *d*) non-diffracting separator layer of thickness t. S, S_1 and S_2 represent the actual and the virtual X-ray sources, respectively. θ is the incidence angle and A_1 and A_2 are the mid-points of the crystalline layer thickness.

the reflectivity will repeat for values of t that satisfy the previous condition, *i.e.* for

$$t = n(d/m)[\sin(\theta_B)/\sin(\theta)], \qquad (6)$$

where m is the reflection order in the Bragg law and θ_B is the Bragg angle. For example, at $\theta = \theta_B$, the reflectivity value of the crystal composed of $p_1 + p_2$ planes will cycle with a period equal to d/m. However, the t values that satisfy (6) will decrease or increase on increasing the deviation of the incidence angle from the Bragg condition. Hence, strictly speaking, the whole RC does not cycle for a typical value of t, even in the case where t equals an integer number of d/m. This is shown in Fig. 2, where the 004 RCs relative to a three-layer silicon structure composed by two outer crystalline layers of equal thickness, $p_1 d = p_2 d = 920d$, are reported for values of the thickness t of the non-diffracting material ranging from zero to $920d$. The calculations refer to non-absorbing layers and hence with q as a real quantity. In Fig. 2, starting from the 004 RC of the perfect crystal of $(p_1 + p_2)d$ planes (Fig. 2*a*), two main effects are observed on increasing the thickness t of the separator layer (Figs. 2*b*–*h*). The first one, for t very small compared with the thickness of the outer crystalline layers (Figs. 2*b* and *c*), is the appearance of fringes with a spacing that is inversely proportional to the total thickness of the new diffracting structure. These fringes are marked on the right-hand side of the RCs in Figs. 2(*b*) and (*c*). On further increasing the thickness of the separator, the second effect begins to appear as a modulation of the interference fringes. This is observed, in the examined angular range of the present example, starting from Fig. 2(*d*), *i.e.* from $t = 64d$. This modulation defines maxima whose spacing is inversely proportional to the thickness of the separator layer. They are marked on the right-hand side of the RCs in Figs. 2(*d*)–(*h*). In Figs. 2(*b*) and (*e*)–(*h*), half-spaced modulation maxima are also visible. It is easy to show, by re-expressing (2) and (5) as a function of the total structure thickness and the separator thickness, that maxima with a spacing inversely proportional to twice

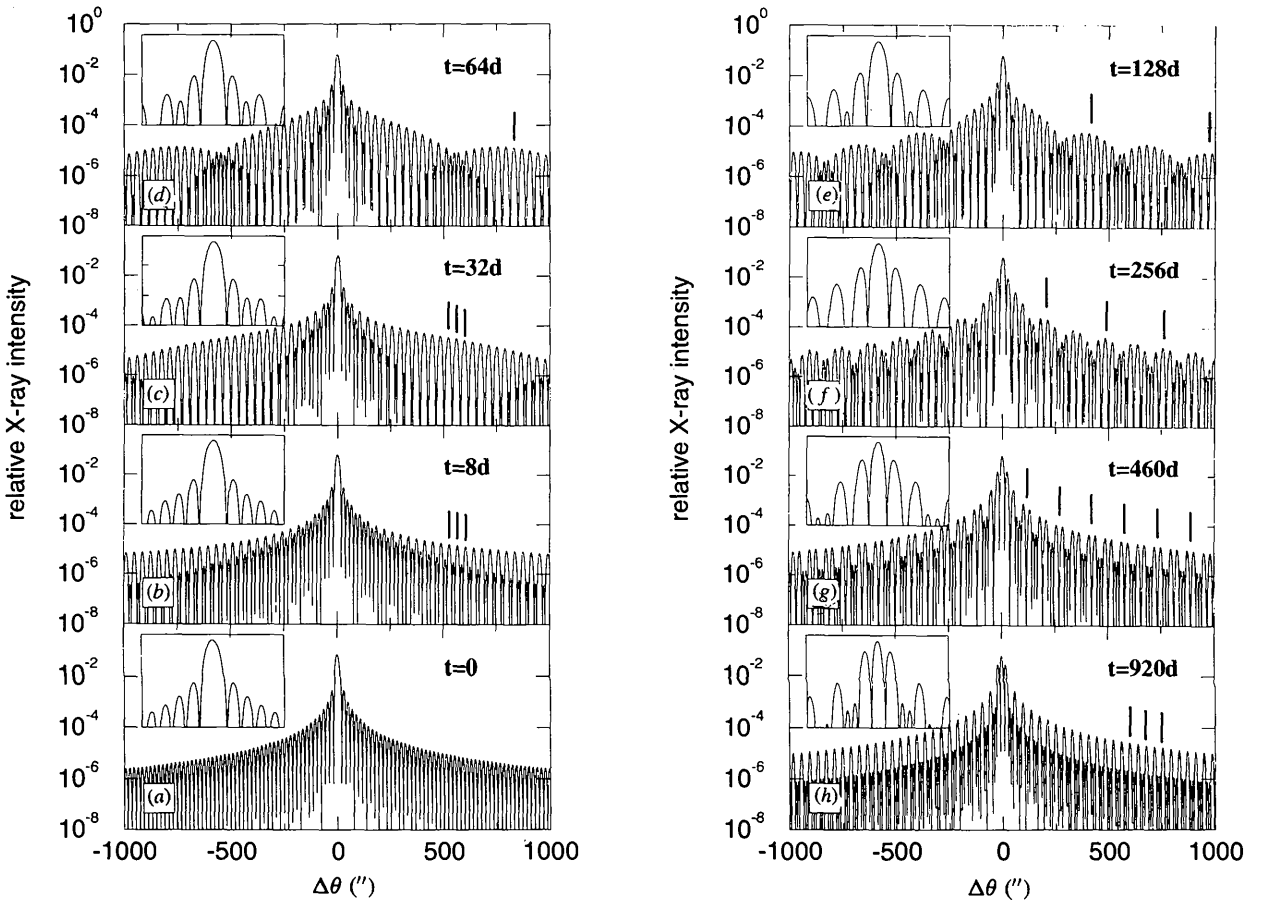

Fig. 2. Interference patterns corresponding to the structure of Fig. 1 for different separator thicknesses $t = nd$ (in-phase condition). The insets are enlarged views of the central spectrum regions from -100 to $100''$ starting from the reflectivity value of 10^{-4}. $\Delta\theta$ is the deviation from the Bragg angle.

these thicknesses have also to be present. Alternatively, in the case of multilayered heterostructures, Tapfer & Ploog (1989) have shown that the difference between the RC resulting from a three-layer heterostructure and the one from a structure with identical outer layers but without a separator is given by the reflectivity of these layers modulated by two sinusoidal functions, which depend on the total and separator thicknesses, respectively. The calculations shown in Fig. 2 are in agreement with this analysis.

When the thickness of the separator layer is not equal to an integer number of spacings d, *i.e.* $t = nd + \Delta d$, taking again the incidence angle $\theta = \theta_B$ as an example, the two outer crystalline layers will be out of phase provided that Δd differs from multiples of d/m. In this case, an additional phase term proportional to $\Delta d/m$ is present in (5), giving rise to a shift of the main diffraction peak. This leads to the possibility of detecting, from the shifts of the Bragg peak, variations of separator thickness of the order of some fraction of d/m, as already outlined by Holloway (1990). The situation is shown in Fig. 3, which reports the RCs obtained on increasing the separator thickness of the corresponding curves in Fig. 2 by a factor $\Delta d/m = d/2m$. This case corresponds to the maximum of the out-of-phase condition and the peak shift leads to a double peak with its central minimum at the Bragg angle (Figs. 3*b*–*h*). The variation of the whole RC on increasing t by keeping $\Delta d/m$ fixed is shown in Figs. 3(*b*)–(*h*). These figures evidence a behaviour similar to that already discussed in the case of Fig. 2. However, it is worthwhile noting that the comparison of Figs. 2 and 3 evidences that the position of the maxima appear to be severely affected by the phase term due to $\Delta d/m$.

The results shown in Figs. 2 and 3, which refer to ideally perfect crystalline structures, evidence that much of the modulations present in the RCs have intensity values in the range 10^{-6} to 10^{-4}. From an experimental point of view, it is expected that, with an open detector double-crystal set-up, normalized intensities smaller than 10^{-4} will be hardly measurable with sufficient accuracy. The insets in Figs. 2 and 3 show reflectivity values

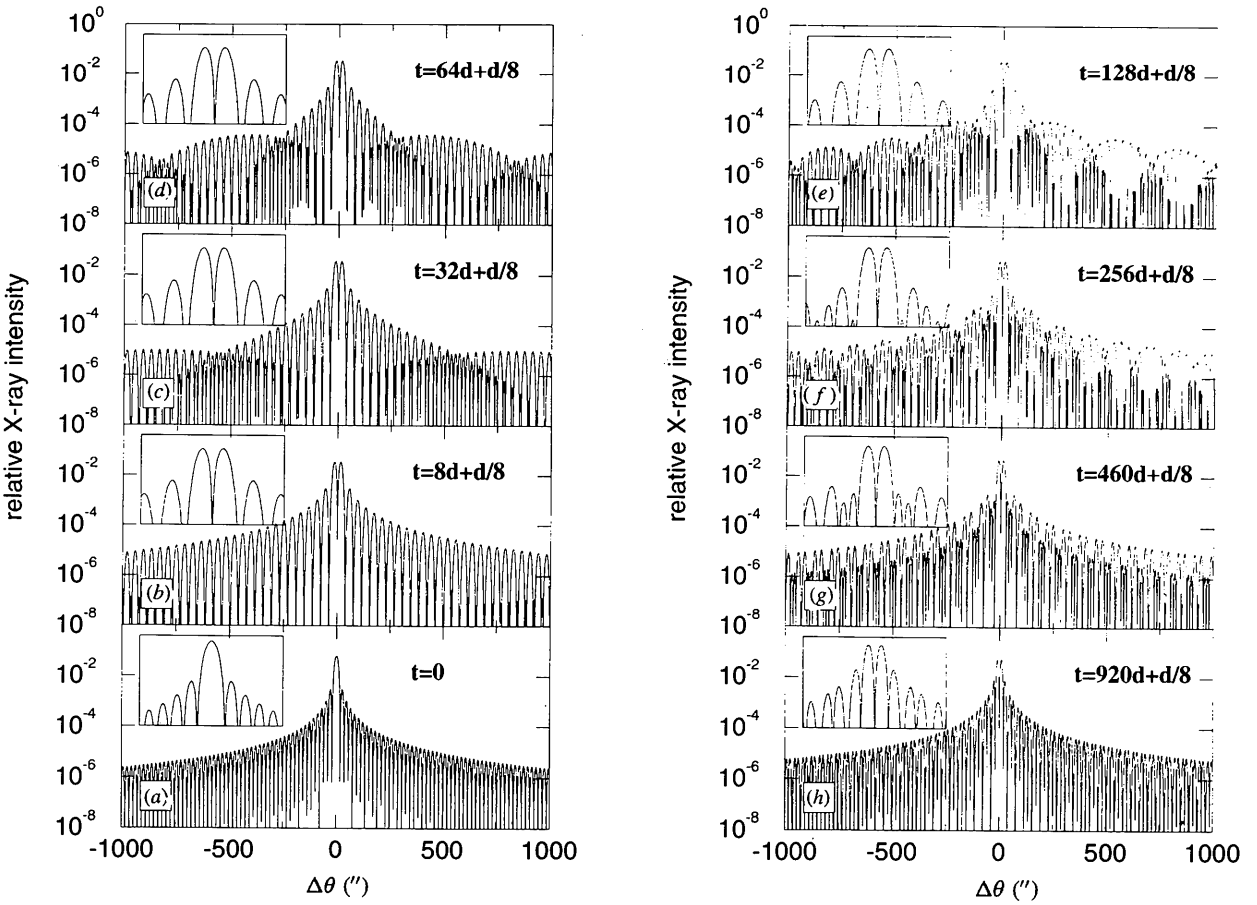

Fig. 3. Interference patterns corresponding to the structure of Fig. 1 for different separator thicknesses $t = nd + d/2m$ (out-of-phase condition). The pattern for $t = 0$ is reported for comparison. The insets are enlarged views of the central spectrum regions from -100 to $100''$ starting from the reflectivity value of 10^{-4}. $\Delta\theta$ is the deviation from the Bragg angle.

starting from 10^{-4} within the angular range from -100 to $100''$ of the corresponding wider spectra. From these insets, it is evident that the possibility of experimentally detecting variations of the separator thickness from the RCs is limited to at least several tens of d, taking also into account that the background due to diffuse scattering will further contribute to obscure the interference effects. Hence, in the case for instance of $t = nd$ (Fig. 2), the RC of a structure with n equal to several tens of d will be hardly distinguishable from that of the perfect crystal with $p_1 + p_2$ planes.

In a previous study, Holloway (1990), on the basis of a similar kinematical analysis of a three-layer heterostructure, claims that, for a layer separation of an integer number of interplanar spacings, the in-phase condition is met, in which case the reflectivity of a lattice of $p_1 + p_2$ planes is recovered, irrespective of the distribution of planes between the two diffracting regions. It should be clear, from our analysis, that this claim is formally incorrect, corresponding to the approximation in (5) of t negligible compared with the thickness $(p_1 + p_2)d$. The same conclusion was drawn by Milita & Servidori (1995), who demonstrated by semikinematical calculations that interference does indeed occur for $t = nd/m$.

Recently, Holloway (1990), Tanner (1993) and Milita & Servidori (1995) stated that cycling of the whole 004 symmetric RC of a (001)-oriented sample occurs when the separator thickness increases by integers of $d/4$, regardless of the fact that the in-phase condition is satisfied. The present analysis evidences that this conclusion corresponds to the further approximation $\theta \simeq \theta_B$ in (6).

In summary, very small separator thickness and incidence angle not far from θ_B are the conditions for which the analyses reported by the other authors are correct. The interest in a more general analysis should be evident if one considers that the thickness threshold beyond which the effects of the separating layer becomes appreciable reduces considerably if an analyser crystal is added in front of the detector (triple-crystal set-up). In this case, in fact, relative intensities in the range 10^{-6} can reliably be measured.

2.2. *Deformed crystal*

This section will address the analysis of samples with buried amorphous (α) layers produced by ion implantation. The reason an ion-implanted sample can be described as a multilayered material is the existence of a depth-dependent damage and strain distribution, as revealed by simulation procedures of calculated kinematical (Speriosu, 1981), semikinematical (Kyutt, Petrashen & Sorokin, 1980) or dynamical (Wie, Tombrello & Vreeland, 1986) RCs to experimental data. These procedures are based on the so-called layer approximation, in which the surface deformed region is divided into a discrete set of layers parallel to the surface. Each layer is characterized by uniform strain perpendicular to the surface ($\varepsilon_\perp$) and uniform value of the static Debye–Waller factor $[\exp(-L_H)]$. Here, $\varepsilon_\perp = (d_\perp - d)/d$ and, in the approximation of a spherically symmetric Gaussian distribution of mean square atomic displacements $\langle w^2 \rangle$ from the lattice sites, $L_H = 8[\pi \sin(\theta_B)/\lambda]^2 \langle w^2 \rangle$. The Debye–Waller factor lowers the structure factor of the corresponding layer with respect to the value for the perfect crystal.

To calculate the interference pattern of an implanted Si crystal by the previous kinematical formalism, (2) and (5) must be extended to the general case of a large number of crystalline layers of different thicknesses, lattice spacings and reflected amplitudes q. This extension is straightforward by recalling the dependence of $\alpha(\theta)$ on the distance $\overline{A_1 A_2}$ shown in Fig. 1 and leads to the following equation:

$$R(\theta) = \sum_{i=1}^{N} \sum_{j=1}^{N} q_i q_j \frac{\sin(p_i \delta_i/2) \sin(p_j \delta_j/2)}{\sin(\delta_i/2) \sin(\delta_j/2)} \times \cos[(4\pi/\lambda) A_{ij} \sin(\theta)], \quad (7)$$

where $q_{i,j}$ are real quantities, N is the number of crystalline layers and A_{ij} is the distance between the mid-points of the layers numbered i and j (Fig. 4). For $N = 2$, $q_i = q_j$ and $\delta_i = \delta_j$, and (7) reduces to equations (2) to (5). Since each layer has its own structure factor in $q_{i,j}$, (7) can be used not only for implanted silicon but also for any multilayered sequence of whichever material. Moreover, separating non-diffracting layers of any thickness can be included.

In the case of a deformed crystal, the simple description of the interference phenomena between d-spaced crystalline layers given in §2.1 is no longer adequate. In general, each layer, characterized by a spacing $d_\perp \neq d$ will also contribute to the total reflectivity with its own Bragg peak, with intensity dependent on the layer thickness. *However, interference phenomena are expected whenever the spacings of layers i and j are very close to each other.* These phenomena are enhanced

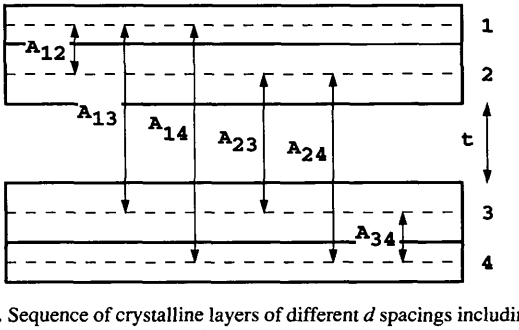

Fig. 4. Sequence of crystalline layers of different d spacings including a non-diffracting separator of thickness t. A_{ij} are the distances between the mid-points of the crystalline layer thicknesses.

on increasing the thickness of the interfering layers as well as when the further condition $p_i \simeq p_j$ is met.

It is to be underlined that the present kinematical theory, unlike previously reported kinematical (or semikinematical) models (Kyutt, Petrashen & Sorokin, 1980; Speriosu, 1981; Wie & Kim, 1991), has led to a simple analytical expression for the *intensity* instead of the *amplitude*. This aspect as well as the more general character of this approach offer the advantages: (i) to treat embedded non-diffracting layers of any thickness in an extended angular range; (ii) to easily expand (7) into the relevant terms for the experimental interference pattern of a complex multilayered structure, as will be shown in the following; and (iii) to use interplanar spacings and not approximated expressions of strain with respect to the substrate. However, we are well aware that considering all the layers (substrate included) as kinematically diffracting materials implies some discrepancies with respect to the experimental RCs. These difficulties cannot be fully overcome by combining kinematical diffraction from the layers and dynamical diffraction from the substrate (Speriosu, 1981; Wie & Kim, 1991) but only by resorting to dynamical theory for all the structure.

3. Comparison between kinematical calculations and experimental results obtained with the dynamical model

3.1. *Experiment and rocking-curve best fit*

(001)-oriented silicon single crystals were implanted at room temperature with doses of (i) 1×10^{15} Si^+ cm^{-2} at 180 keV; (ii) 2.5×10^{14} As^+ cm^{-2} at 800 keV; (iii) 1.5×10^{15} Si^+ cm^{-2} at 1.5 MeV. These conditions ensure the formation of buried α layers.

The X-ray measurements were made with a double-crystal diffractometer arranged in parallel (non-dispersive) Bragg–Bragg $(n, -n)$ geometry with an open window detector. Cu $K\alpha_1$ radiation was used from a conventional sealed tube. The collimator was a silicon single crystal asymmetrically cut for grazing-incidence 004 reflection, giving a probe beam on the sample with a divergence in the scattering plane as low as about 2 μrad. This value is ten times smaller than the intrinsic width of the symmetric 004 RC of an infinitely thick silicon crystal and therefore enables convolution to be neglected when minimization routines are used to best fit the experimental X-ray intensity profiles. Hence, the calculated RC of the sample was obtained by simply averaging its σ- and π-polarization profiles over the weights of the σ and π integrated intensities from the collimator. The calculated weights for σ and π integrated intensities at the exit from the collimator are $w_\sigma = 0.8049$ and $w_\pi = 0.1951$.

The RC best fits were made by using the dynamical formalism proposed by Wie *et al.* (1986) for a laminar structure of the sample. The initial damage distribution was tailored on the basis of the implant parameters by using a model for which the strain values in the laminae are to some extent constrained to follow a physically plausible depth profile. This precaution is necessary to strongly reduce the probability that unreasonable saw-toothed profiles are obtained when the lamina strains are free to vary independently of one another. This starting profile was then optimized automatically by means of a simplex-type routine (Press, Teukolsky, Vetterling & Flannery, 1992), which minimizes the differences between experimental (I_i^{exp}) and calculated (I_i^{calc}) intensities. The criterion

$$\chi^2 = (1/k) \sum_{i=1}^{k} [\log(I_i^{calc}/I_i^{exp})]^2$$

was used, where k is the number of experimental points. The diffuse scattered intensity, unavoidably collected in the absence of a crystal analyser between sample and detector, was taken into account by a Lorentzian-type distribution, following the method previously described (Servidori & Cembali, 1988).

3.2. *Results and discussion*

Figs. 5, 6 and 7 show the 004 RC best fits and the corresponding $\varepsilon_\perp$ and L_H profiles for the three implanted samples. In Fig. 5(*b*), error bars in the $\varepsilon_\perp$ and L_H profiles are reported to represent the accuracy of the depth distribution of these quantities. The method used to evaluate the bars was a Monte Carlo error analysis very similar to that applied by Ellis & Freeman (1995) to extended X-ray fine-structure data.

The positive values of $\varepsilon_\perp$ indicate a strong effect of the interstitial-type defects produced by the implant. These defects also displace the Si atoms from the ideal sites in the surrounding regions of the matrix ($L_H > 0$). The buried α layers are easily recognized by the dip in the strain profile and by the strong value of L_H. In a previous paper (Milita & Servidori, 1995), it was shown that lamina thickness (t_o) and strain ($\varepsilon_\perp$), the most important input parameters in computing RCs, should be handled by the calculation code in different ways according to whether they refer to a crystalline or an α lamina. For a crystalline lamina, the effective thickness for RC calculation is $t = t_o(1 + \varepsilon_\perp)$, where $t_o = nd/4$ is the thickness in the absence of deformation and $t_o\varepsilon_\perp = (n\Delta d/d)d/4$ is the strain-induced correction to t_o. For n large, this correction can be greater than $d/4$ and can be written in the general case as

$$t_o\varepsilon_\perp = (l + x)d/4,$$

where l is an integer $(0, 1, 2, \ldots)$ and $0 \leq x < 1$ (for $l = x = 0$ the situation of the perfect lamina is obtained). In the crystalline case, different RCs are obtained for different l values.

Similarly, in the case of an embedded α lamina produced by ion implantation, an expansion of the implanted crystal $(l + x)d/4$ can be experimentally measured by mechanical devices, such as alpha step or cross-sectional transmission electron microscopy. However, in the experimental RCs, the relationship with the number of crystal planes pre-existing the amorphization process is obviously completely lost and the diffraction pattern will depend on the spacing of the interfering layers and the actual separator thickness t as shown in (7). Hence, for embedded α laminae, one has to consider $t = t_{o\alpha}(1 + \varepsilon_{\perp\alpha})$, with $t_{o\alpha} = (n + l)d/4 = n'd/4$ and the strain-induced correction to $t_{o\alpha}$ as $t_{o\alpha}\varepsilon_{\perp\alpha} = xd/4$. It is to be emphasized that the condition $\varepsilon_{\perp\alpha} = 0$, being related to the spacing d of the substrate, does not imply a lattice phase matching of the deformed layers external to the separator. In fact, these layers have spacings $d_\perp$ different from one another and from d, so that one should speak merely of a rigid outward translation due to the implanted layer equal to a multiple of $d/4$.

The thicknesses $t_{o\alpha} = n'd/4$ and the strains $\varepsilon_{\perp\alpha} = x/n'$ are the quantities obtained by best fit for the α layers and are evident in the figures. It is interesting to note that in the case of silicon implanted with Si^+ ions at 180 keV and 1.5 MeV, the value of $\varepsilon_{\perp\alpha}$ is essentially zero (see Figs. 5*b* and 7*b*) corresponding to a rigid translation of a multiple of $d/4$. As for L_H, values often higher than 100 were obtained by best fit. However, the value $L_H = 5$ was reported in Figs. 5 to 7 for the sake of representation because it is sufficiently large to reduce the structure factor of the layer to such a small value as to make it non-diffracting.

In general, in ion-implanted materials containing embedded α laminae, the analysis of the interference modulations observed in the experimental RCs is very complex. In the framework of the layer approximation, this can be understood by saying that, owing to the presence of a strain distribution, several pairs of deformed layers can contribute to the overall interference modulation. However, it was shown in §2.1 that, in the simplest case of a *thick* amorphous layer between two crystals of d spacing and equal thickness, the angular distance of the interference modulations is inversely proportional to twice the separator thickness. Therefore, in the experimental situation, interference fringes with a spacing inversely proportional to approximately twice the amorphous layer thickness will be expected when-

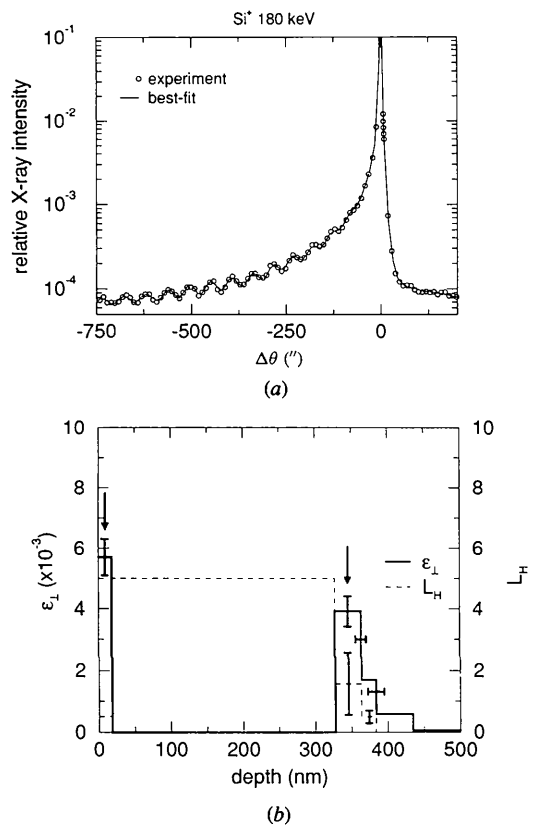

Fig. 5. (*a*) Experimental and best-fitted RCs and (*b*) strain and static disorder profiles for the sample implanted with 180 keV Si^+ ions. In (*b*), the bars indicate the estimated errors in the values of thickness, strain and static disorder. $\Delta\theta$ is the deviation from the Bragg angle of the substrate corrected for refraction.

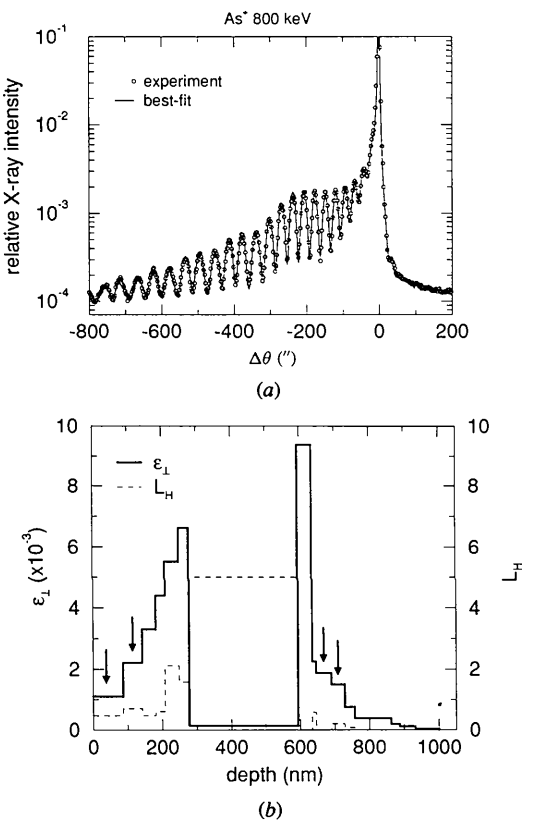

Fig. 6. (*a*) Experimental and best-fitted RCs and (*b*) strain and static disorder profiles for the sample implanted with 800 keV As^+ ions.

ever the interference term due to the three-layer structure composed of the amorphous and the two adjacent crystalline layers is the main contribution to the reflectivity modulations. This is the case for the RCs shown in Figs. 5(*a*) and 7(*a*). In fact, from the average fringe spacings of 55 and 45″ deduced from these figures, respectively, calculations of the interference maxima positions, based on (5), give separator thicknesses of 350 and 430 nm, respectively, in qualitative agreement with those of the amorphous layers shown in Figs. 5(*b*) and 7(*b*). On the contrary, for the RC shown in Fig. 6(*a*), the average interference fringe spacing of 35″ corresponds to a separator thickness of 500 nm, in striking contrast with that of the amorphous layer shown in Fig. 6(*b*). In this case, the corresponding strain distribution shown in Fig. 6(*b*) evidences very different spacings as well as high strain values of the crystalline layers adjacent to the amorphous lamina, thus suggesting that interference modulations arising from this structure are negligible in the angular range shown in Fig. 6(*a*). These qualitative observations are confirmed by an analysis of the main interference terms responsible for the observed interference modulations, which, on the basis of kinematical [(7)] or dynamical (Wie *et al.*, 1986) calculations, allows one to locate the corresponding

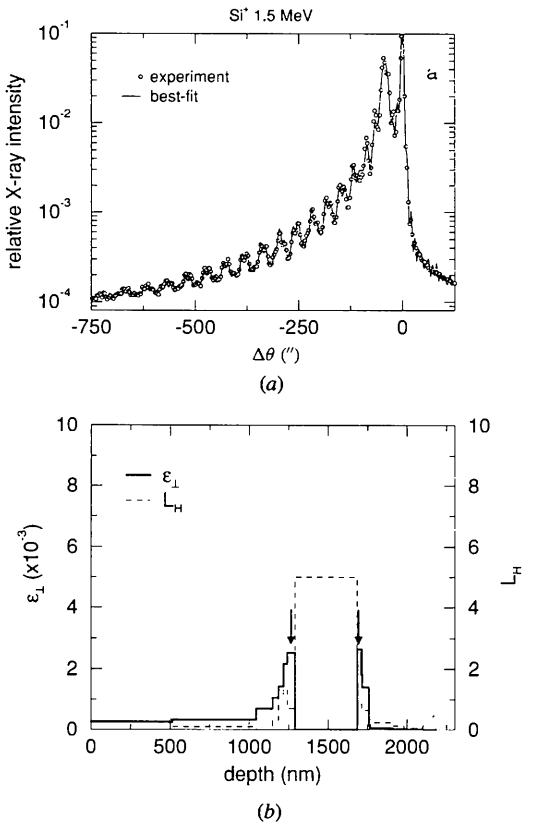

Fig. 7. (*a*) Experimental and best-fitted RCs and (*b*) strain and static disorder profiles for the sample implanted with 1.5 MeV Si^+ ions.

interfering layers. These layers are marked by arrows in Figs. 5(*b*), 6(*b*) and 7(*b*). From this analysis, as noted above, it is apparent that the RCs shown in Figs. 5 to 7 are typical of different interference phenomena among the deformed layers of the implanted crystals. In Fig. 6(*b*), it is shown that, unlike the case of Figs. 5(*b*) and 7(*b*), the strongly interfering layers are located at the surface and in the tail of the strain distribution.

Figs. 8 to 10 show a comparison of the RCs obtained for the three samples with a dynamical model with those calculated by the kinematical approach. For comparison, the data of each layer in Figs. 5 to 7 were introduced in (7), *i.e.* thickness of the crystalline layers as integers of $d_\perp/4$ with $d_\perp/4 > d/4$, as deduced from $\varepsilon_\perp$, thickness of the α layers and lamina structure factors as modified by the static Debye–Waller factors $\exp(-L_H)$. Moreover, a perfect silicon layer of thickness $5 \times 10^5 d/4$ was added to the bottom of the sequence to simulate the presence of the substrate and the distribution of the diffuse scattering under the diffracted intensity was removed. The kinematical calculation combined the σ- and π-polarization components according to the weights w_σ and w_π reported in §3.1. From Figs. 8 to 10, where the obvious substrate peak intensity greater than 1 for the kinematical case is not shown, it can be observed that, apart from an intensity overestimate in the positive angular side of the RC and the narrow fringe spacing due to the thick substrate, (7) is able to describe correctly the interference phenomena occurring in the multilayer structure. All interference fringes and their modulations are well reproduced. The intensity depletion at $\Delta\theta > 0$ results from dynamical interaction between waves scattered from the expanded surface layers and the thick perfect substrate (Afanas'ev, Koval'chuk, Lobanovich, Imamov, Aleksandrov & Melkonyan, 1981).

4. Conclusions

This paper reports a kinematical approach for the description of symmetric Bragg-case interference phenomena occurring in multilayered structures. The formalism is different from those already reported in the literature for structures having such thin embedded crystalline layers that diffraction from them can be neglected. In fact, it can be used for any layer sequence, including non-diffracting materials of any thickness. Its more general validity is demonstrated by comparison with rocking curves obtained by dynamical best fit of experimental data relative to implanted silicon. The comparison shows an excellent agreement with all the interference features present in the experimental rocking curves. Finally, it is worthwhile noting that the form of the kinematic expression (7) appears well adapted to an extension of the model to double-crystal X-ray dispersive configurations by taking also in consideration the coherence depth of the X-radiation. This will be the subject of future work.

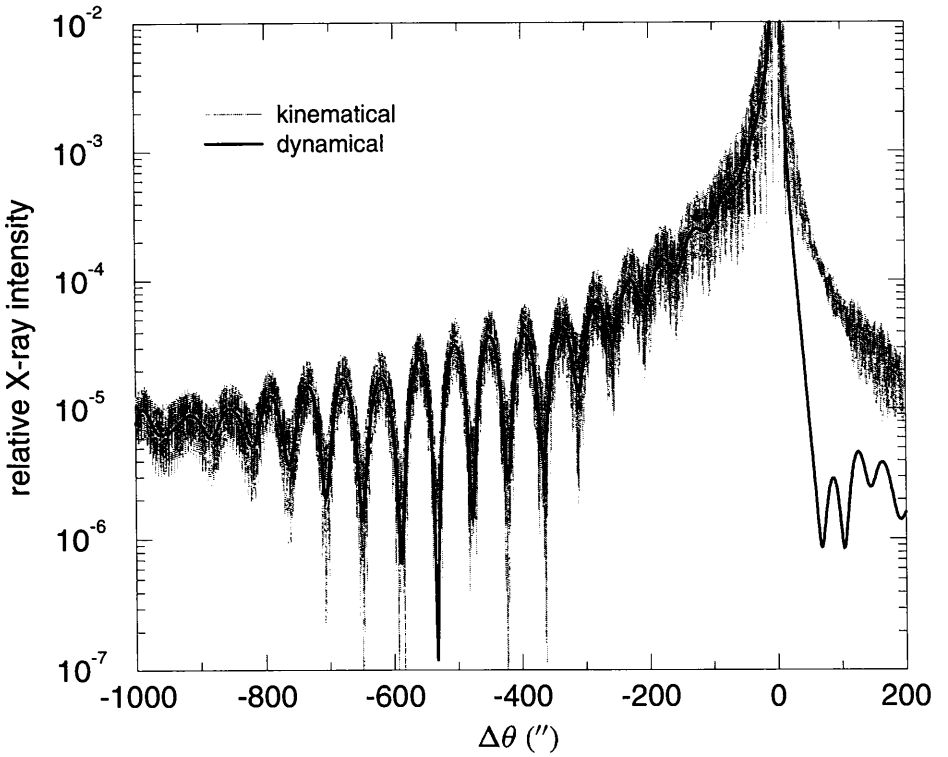

Fig. 8. Comparison between kinematical and dynamical RCs of the sample implanted with 180 keV Si^+ ions.

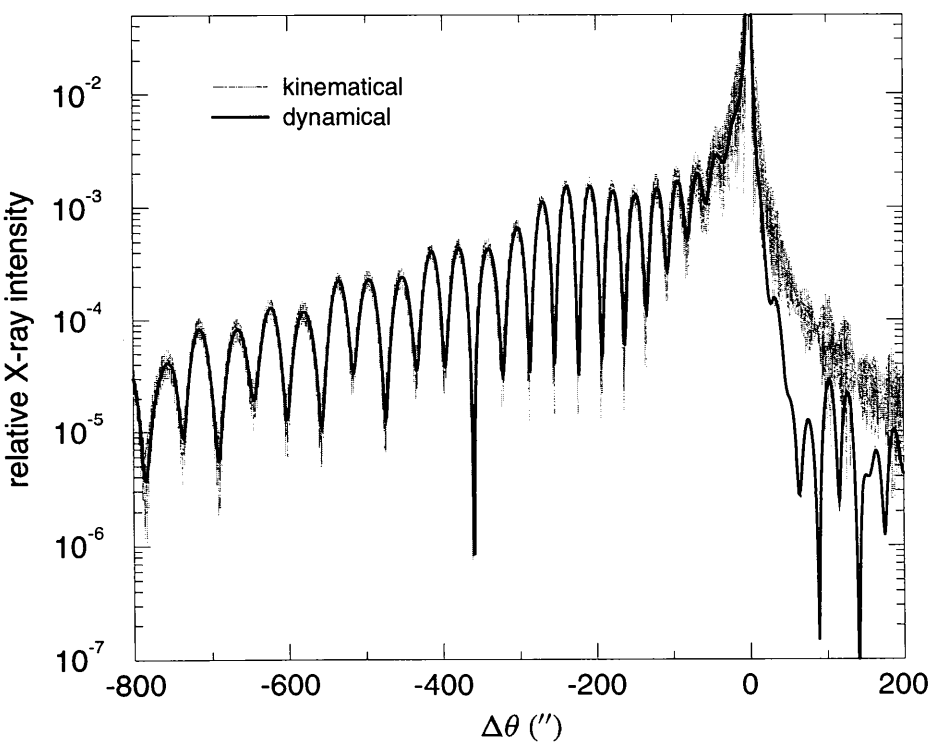

Fig. 9. Comparison between kinematical and dynamical RCs of the sample implanted with 800 keV As^+ ions.

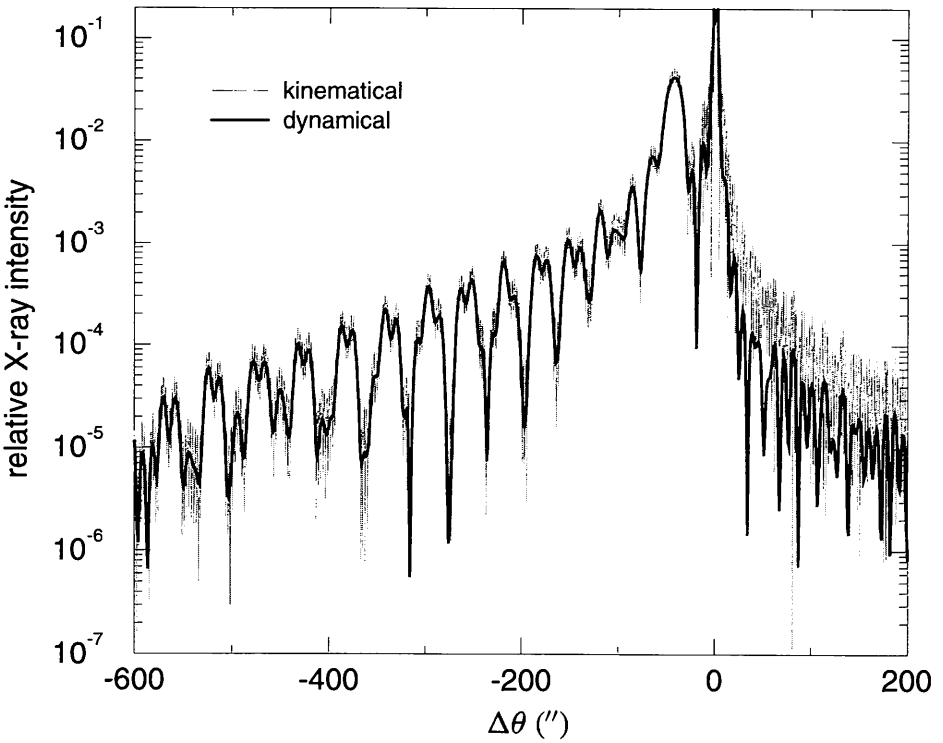

Fig. 10. Comparison between kinematical and dynamical RCs of the sample implanted with 1.5 MeV Si^+ ions.

References

Afanas'ev, A. M., Koval'chuk, M. V., Kovev, E. K. & Kohn, V. G. (1977). *Phys. Status Solidi A*, **42**, 415–422.

Afanas'ev, A. M., Koval'chuk, M. V., Lobanovich, E. F., Imamov, R. M., Aleksandrov, P. A. & Melkonyan, M. K. (1981). *Sov. Phys. Crystallogr.* **26**, 13–17.

Ellis, P. J. & Freeman, H. C. (1995). *J. Synchrotron Rad.* **2**, 190–195.

Holloway, H. (1990). *J. Appl. Phys.* **67**, 6229–6236.

James, R. W. (1967). *The Optical Principles of the Diffraction of X-rays*, edited by W. L. Bragg, ch. 2. London: G. Bell and Sons.

Jaussaud, C., Stoemenos, J., Margail, J., Papon, A. M. & Bruel, M. (1991). *Vacuum*, **42**, 341–347.

Kyutt, R. N., Petrashen, P. V. & Sorokin, L. M. (1980). *Phys. Status Solidi A*, **60**, 381–389.

Margail, J., Lamure, J. M. & Papon, A. M. (1992). *Mater. Sci. Eng.* **B12**, 27–36.

Milita, S. & Servidori, M. (1995). *J. Appl. Cryst.* **28**, 666–672.

Nikulin, A. Yu., Snigirev, A. A., Starkov, V. V., Hemment, P. L. E. & Vyatkin, A. F. (1992). *Mater. Sci. Eng.* **B13**, 287–290.

Press, W. H., Teukolsky, S. A., Vetterling, W. T. & Flannery, B. P. (1992). *Numerical Recipes in Fortran.* Cambridge University Press.

Servidori, M. & Cembali, F. (1988). *J. Appl. Cryst.* **21**, 176–181.

Speriosu, V. S. (1981). *J. Appl. Phys.* **52**, 6094–6103.

Tanner, B. K. (1993). *J. Phys. D*, **26**, A151–A155.

Tapfer, L. & Ploog, K. (1989). *Phys. Rev. B*, **40**, 9802–9810.

Wie, C. R. (1989). *J. Appl. Phys.* **65**, 1036–1038.

Wie, C. R., Chen, J. C., Kim, H. M., Liu, P. L., Choi, Y. W. & Hwang, D. M. (1989). *Appl. Phys. Lett.* **55**, 1774–1776.

Wie, C. R. & Kim, H. M. (1991). *J. Appl. Phys.* **69**, 6406–6412.

Wie, C. R., Tombrello, T. A. & Vreeland, T. Jr (1986). *J. Appl. Phys.* **59**, 3743–3746.